

Nuclear clustering in light neutron-rich nuclei

Yang Liu¹ · Yan-Lin Ye¹

Received: 1 September 2018 / Revised: 15 November 2018 / Accepted: 16 November 2018 / Published online: 27 November 2018
© Shanghai Institute of Applied Physics, Chinese Academy of Sciences, Chinese Nuclear Society, Science Press China and Springer Nature Singapore Pte Ltd. 2018

Abstract Clustering is a general phenomenon observed in light nuclei, especially in neutron-rich nuclei in which molecular configurations can be formed with various combinations of valence neutrons. Thus far, many theoretical models have been developed to describe nuclear clustering phenomena. These models are outlined in this review article, with an emphasis on their basic formulations and physical ingredients. In addition, various experimental tools, such as inelastic excitation and decay, transfer reactions, and resonant scattering reactions, have been applied to investigate the cluster structures inside the nucleus. Each tool possesses certain advantages and favorable applications, which are also described. In the case of neutron-rich nuclei, cluster structures may be configured as molecular states that form rotational bands with an extremely large moment of inertia and generate relatively large cluster decay width. The major experimental criteria for the identification of cluster formation are discussed herein.

Keywords Microscopic cluster models · Rotational band · Decay width · Monopole transition strength · Selective decay patterns

This work was supported by the National Key R&D Program of China (No. 2018YFA0404403) and the National Natural Science Foundation of China (Nos. 11535004, 11875074, 11875073, 11775004, 11775013, 11775316).

✉ Yan-Lin Ye
yeyl@pku.edu.cn

¹ School of Physics and State Key Laboratory of Nuclear Physics and Technology, Peking University, Beijing 100871, China

1 Introduction

Clustering is one of the most striking phenomena in the matter universe, owing to the fact that it exists not only on the largest physical scale such as the star systems [1] but also on the smallest scale like the quark clustering in hadron systems [2]. In the subatomic domain, nucleon clustering has brought in another fresh perspective of the fundamental structure inside nuclei [3–9], which differs conceptually from the traditional standpoint of the independent-particle model. Furthermore, cluster formation has played a significant role in the understanding of the nucleosynthesis in stellar evolution [10]. A typical example is the well-known Hoyle state [11] which is the key portal for the synthesis of ^{12}C , the crucial requisite of a human being.

The alpha cluster model, first proposed by Wheeler and Margenau [3, 4], provides the initial description of nuclear clustering. In fact, the α -particle has the largest binding energy per nucleon among its neighboring nuclei and its first excited state is as large as 20 MeV, in favor of its persistence inside a nucleus. In self-conjugate $4N$ light stable nuclei ($N = Z$ even–even nuclei), the rotational bands with an $\alpha + X$ bimolecular structure are located methodically near the threshold energies with which the nuclei can decay into the corresponding sub-clusters [12]. Based on this strong correlation, Ikeda suggested an illustrative diagram to explicate the relevant cluster structures around the corresponding threshold energies [6]. Subsequently, remarkable progress has been made in this field from the theoretical as well as experimental points of view [13, 14].

In order to depict the internal structures of the non- α -conjugate neutron-rich unstable nuclei, a new threshold

diagram [7] is needed to deal with the extra degree of freedom brought by the valence neutrons surrounding the cluster cores [15]. The extra covalent neutrons are expected to increase the binding energy so as to help in stabilizing the whole system [8], in a manner similar to the electrons in covalent atomic molecules [16]. Considerable efforts have been made to investigate this new phenomenon, and tremendous progress has been achieved in the case of neutron-rich beryllium and carbon isotopes.

As the α - α dumbbell cluster structure of ^8Be [17] is well established, the neutron-rich beryllium isotopes from ^9Be to ^{12}Be are typical examples to explore the cluster structures with valence neutrons. Multifarious molecular structures with the $2\alpha + Xn$ configuration have been studied both theoretically [18–25] and experimentally [26–32]. By analogy, it is reasonable to extend the studies to the neutron-rich carbon isotopes, inside which three tightly bound α -cores may be existent [33] that form unusual configurations such as the chain structures. Even though ^{12}C without excess neutrons does not possess a linear-chain structure, the valence neutrons around it may help to increase the binding energy and maintain the linear-chain framework [34–43].

In this review article, recent theoretical and experimental progress in the study of nuclear clustering in light neutron-rich nuclei is presented, with some focus on the neutron-excess beryllium and carbon isotopes. The article is organized as follows: In Sect. 2, a theoretical description is given of the cluster phenomenon inside a nucleus from the viewpoints of various cluster models such as the resonating group method (RGM), generator coordinate method (GCM), orthogonality condition method (OCM), molecular-orbit model (MO), generalized two-center cluster model (GTCM), and antisymmetrized molecular dynamics (AMD). In Sect. 3, the experimental investigation of a cluster state with various reaction tools, such as the inelastic excitation and decay, transfer reactions, and resonant scattering reactions is discussed. The experimental evidence of the cluster formation in neutron-rich beryllium (^{10}Be , ^{12}Be) and carbon isotopes (^{13}C , ^{14}C) is demonstrated in detail. In Sect. 4, a brief summary is given.

2 Theoretical description

2.1 Resonating group method

Microscopic cluster models have been employed to study the cluster structures of light nuclei since the early 1960s. Generally, the Hamiltonian of the A -nucleon system can be written as

$$H = \sum_{i=1}^A \frac{\vec{p}_i^2}{2m} + \sum_{i>j=1}^A V_{ij}(\vec{r}_i - \vec{r}_j), \quad (1)$$

where \vec{p}_i is the momentum vector of the nucleon i , \vec{r}_i and \vec{r}_j are the space coordinates of the nucleons i and j , respectively, V_{ij} is the nucleon–nucleon interaction potential which contains both the Coulomb and nuclear terms (central and spin–orbit terms) [44], and m represents the nucleon mass. Taking into consideration the computational complexity of solving the Schrödinger equation with large nucleon numbers ($A > 4$), the cluster approximation, under which the A -nucleon system is divided into two separated sub-clusters, may be adopted. This approximation was introduced by Wheeler in the resonating group method (RGM) [3].

The RGM wave function for two-cluster systems can be expressed as [45]

$$\psi(\vec{r}_1, \vec{r}_2, \vec{r}) = \mathcal{A}_T \phi_1(\vec{r}_1) \phi_2(\vec{r}_2) \chi(\vec{r}), \quad (2)$$

where \vec{r}_1 and \vec{r}_2 are the coordinates of the center of mass (c.m.) of the two ingredient clusters, $\vec{r} = \vec{r}_1 - \vec{r}_2$ is the relative coordinate, $\phi_i(\vec{r}_i)$ represents the internal wave function, and $\chi(\vec{r})$ is the relative wave function describing the inter-cluster relative motion which can be deduced by the energy variation [46]. \mathcal{A}_T is the total antisymmetrizer of all the nucleons that is given by

$$\mathcal{A}_T = \mathcal{A} \mathcal{A}_1 \mathcal{A}_2, \quad (3)$$

where \mathcal{A}_i represents the antisymmetrizer of the nucleons inside one cluster and \mathcal{A} describes the antisymmetrizer between the two clusters. It may be noted that the RGM calculations can provide an explanation not only for the cluster states but also for the single-particle states [47], on account of the total antisymmetrizer \mathcal{A}_T , which makes it possible for a resonant exchange of nucleons between the groups.

Tang and LeMere have applied the RGM calculations to investigate the bound and resonant states of ^{17}O , ^{18}F , ^{19}F and ^{20}Ne , with a predominant $X + ^{16}\text{O}$ configuration [48]. The calculated levels agree quite well with the previous experimental results [49], which indicate the existence of $X + ^{16}\text{O}$ cluster structure in these nuclear systems.

2.2 Generator coordinate method

In spite of the success of the RGM in depicting the inter-cluster relative motion, there is still an enormous challenge in dealing with heavier systems or multichannel problems which would entail tedious calculations in separating the internal and relative coordinates with antisymmetrization. This difficulty could not be resolved until the adoption of

the generator coordinate method (GCM) [45, 50] with the Bloch–Brink cluster wave function.

The relative wave function $\chi(\vec{r})$ in GCM is expanded over some Gaussian functions that are centered at different generated coordinates. As a consequence, the total GCM wave function $\psi(\vec{r}_1, \vec{r}_2, \vec{r})$ can be expressed as a superposition of the Slater determinants [50], which signifies that the computational complexity can be reduced to such an extent that the investigation of the cluster structures in heavy systems becomes a feasible issue.

The one-cluster Slater determinants with A_1 nucleons located at a common position \vec{S} can be defined as

$$\psi_1(\vec{S}) = \frac{1}{\sqrt{A_1!}} \mathcal{A}_1 \phi_1(\vec{r}_1, \vec{S}) \dots \phi_{A_1}(\vec{r}_1, \vec{S}), \tag{4}$$

where the single-nucleon wave function $\phi_1(\vec{r}_1, \vec{S})$ (neglecting the spin and isospin components) is a harmonic-oscillator function. Therefore, Eq. (4) can be rewritten as [51]

$$\psi_1(\vec{S}) = \exp\left(-\frac{A_1}{2b^2}(\vec{r}_1 - \vec{S})^2\right) \phi_1(\vec{r}_1), \tag{5}$$

where $\phi_1(\vec{r}_1)$ is the same as that in Eq. (2) and b is the oscillator parameter which is uniform for all the nucleons. Thus, the two-center wave function located at \vec{r}_1 and \vec{r}_2 of the A -nucleon system can be written as

$$\psi(\vec{R}) = \frac{1}{\sqrt{N}} \mathcal{A} \psi_1\left(-\frac{A_2}{A} \vec{R}\right) \psi_2\left(\frac{A_1}{A} \vec{R}\right), \tag{6}$$

where $\vec{R} = \vec{r}_1 - \vec{r}_2$ is the generator coordinate whose origin is located at the c.m. and N is the normalization factor. With the combination of Eqs. (5) and (6), the Slater determinants can be rewritten as

$$\psi(\vec{R}) = \frac{1}{\sqrt{N}} \psi_{\text{cm}}(\vec{R}) \mathcal{A} \phi_1(\vec{r}_1) \phi_2(\vec{r}_2) \Gamma(\vec{R}, \vec{R}), \tag{7}$$

where $\psi_{\text{cm}}(\vec{R})$ describes the motion of the c.m. and $\Gamma(\vec{R}, \vec{R})$ is the radial wave function. The calculation of the GCM matrix elements becomes more concise with the separation of the motion of the c.m. as only simple Gaussian functions are involved in Eq. (7) [52].

In the case of overlapped clusters, the wave function in Eq. (7) would be equivalent to the shell-model wave function owing to the antisymmetrization of the nucleons among the clusters. However, if the distance between the clusters is large enough to ignore the inter-cluster antisymmetrization, the wave function in Eq. (7) effectively describes the real cluster structure.

Descouvemont performed a simultaneous analysis of the ${}^9, {}^{10}, {}^{11}\text{Be}$ isotopes with the $2\alpha + Xn$ multi-cluster GCM calculation and anticipated the decrease in the alpha-clustering effect from ${}^9\text{Be}$ to ${}^{11}\text{Be}$ [53]. In a similar study, he

predicted a strong mixing of the ${}^6\text{He} + {}^6\text{He}$ and ${}^4\text{He} + {}^8\text{He}$ configurations, rather than a dominant ${}^6\text{He} + {}^6\text{He}$ structure, in ${}^{12}\text{Be}$ [54].

2.3 Orthogonality condition method

The orthogonality condition method (OCM) was proposed by Saito [45, 55] as a simplified approach to deal with the role of the Pauli principle in the interaction between clusters. It gives rise to the characteristic energy-independent, but angular-momentum-dependent, inner oscillation for the solution of the relative wave function $\chi(\vec{r})$ in Eq. (2). In OCM calculations, the relative wave function between the clusters is required to be orthogonal to the Pauli forbidden states (PFS), ensuring that the interaction takes effect only in the physical space orthogonal to the PFS under antisymmetrization. Considering the Pauli principle, the projection operator is defined as follows [55]

$$\Lambda = 1 - \sum_{i \in \text{PFS}} |\varphi_i\rangle \langle \varphi_i|, \tag{8}$$

where $|\varphi_i\rangle$ are the PFS which can be derived from the internal configurations of the component clusters. It is obvious that $\Lambda|\varphi_i\rangle = 0$. Hence, the Schrödinger equation for the OCM can be deduced as [45]

$$\Lambda(E_{\text{rel}} - T - V_{\text{eff}})\Lambda|\chi(\vec{r})\rangle = 0, \tag{9}$$

where E_{rel} denotes the relative energy in the c.m. system, T is the kinetic operator and V_{eff} is the local potential regarded as the average potential between the two clusters. Since $|\varphi_i\rangle$ are redundant solutions of Eq. (9), it can be rewritten as

$$(E_{\text{rel}} - T - V_{\text{eff}})|\chi(\vec{r})\rangle = - \sum_i |\varphi_i\rangle \langle \varphi_i| T + V_{\text{eff}} |\varphi_i\rangle, \tag{10}$$

where the relative wave function $|\chi(\vec{r})\rangle$ permanently complies with the orthogonality condition $\langle \varphi_i | \chi(\vec{r}) \rangle = 0$.

The OCM was applied extensively to study the nuclear clustering structures. For example, Matsuse and Kamimura [56] concluded that the first $K^\pi = 0^-$ band in ${}^{20}\text{Ne}$ had a strong α -clustering character, whereas the ground state band possessed the shell-model like structure preferably, based on the quantitative computation of the α -width and spectroscopic factors with OCM.

A certain amount of progress was made toward resolving the multi-cluster problem by Horiuchi [57], wherein the binding energy and excited levels of ${}^{12}\text{C}$ were reproduced by using an extended 3α OCM model. It was found that the ground state had a shell-model-like configuration, whereas the excited 0^+ state had a well-developed molecular-like

structure. Various multi-cluster OCM calculations have been carried out [58] since then.

Yamada [59] adopted a four-body $3\alpha + n$ OCM theory to study the changes in the configurations of ^{13}C brought about by the additional valence neutrons and determined the monopole transition strength of the low-lying states below the $3\alpha + n$ threshold. It was clear that the monopole matrix elements of the four lowest $1/2^-$ states above the ground state were much stronger than the single-particle state, indicating the dominant $^9\text{Be} + \alpha$ cluster structures in these states. The latest experiment of ^{13}C conducted by Feng et al. [40] has established an enhanced monopole matrix element of $(6.3 \pm 0.6) \text{ fm}^2$ for the $14.3 \text{ MeV } (1/2_5^-)$ state, which is in good agreement with the prediction of the OCM calculations.

In addition, Yamada extended the OCM calculations to the four- α -particle condensate state in ^{16}O , and the results of the calculations in six of the lowest $J^\pi = 0^+$ states are in excellent agreement with the experimental spectrum [60]. The 0_6^+ state residing in $\sim 2 \text{ MeV}$ above the four- α -particle breakup threshold has a large α condensate fraction of 61% as well as a large component of $\alpha + ^{12}\text{C}(0_2^+)$ configuration. This brings a new perspective on the experimental endeavor to explore the α -particle condensation state in ^{16}O .

2.4 Molecular-orbit model

As the $\alpha + \alpha$ dumbbell cluster structure of ^8Be is well established [17], it is logical to treat the neutron-rich beryllium isotopes as typical molecular structures with valence neutrons moving around the two cluster-cores. In the molecular-orbit model (MO), the orbits of the valence neutrons are constructed from a succinct linear combination of the cluster orbits (LCCO) [21, 23, 61].

Neglecting the spin-orbit coupling, the spatial part of the MO function $|\lambda\rangle$ is expanded by the orthogonal basis vector $|\alpha\rangle$, constructed with the cluster orbits. $|\lambda\rangle$ can be defined as

$$|\lambda\rangle = \sum_{\alpha} C_{\lambda\alpha} |\alpha\rangle, \tag{11}$$

where $C_{\lambda\alpha}$ can be determined by using the Hartree-Fock equation and the basis vector $|\alpha\rangle$ can be written as

$$|\alpha\rangle = \sum_{m,A} D_{\alpha mA} |m; A\rangle, \tag{12}$$

where $|m; A\rangle$ are the cluster orbits for which the harmonic-oscillator wave functions are applied for convenience and $D_{\alpha mA}$ are determined by a classification using an irreducible representation of an assumed point group symmetry and an orthogonalization among orbits belonging to the same representation [17].

Okabe and Abe succeeded in extending the MO model to the odd- A system ^9Be [21, 61], proposing that the degree of clustering in ^9Be depends crucially on the motions of the valence neutrons. The properties of the low-lying levels of ^9Be are reproduced satisfactorily with the MO model. Itagaki et al. [35] carried out excellent work in describing the neutron-rich carbon isotopes with the well-developed 3α -cluster MO model, suggesting configurations of two neutrons in the σ orbits and two in the π orbits, for the excited states in ^{16}C .

2.5 Generalized two-center cluster model

Although the MO model was reasonably successful in reproducing the unusual low-lying states of the light neutron-rich nuclei, there was a difficulty in describing the highly excited states above the particle-decay threshold. Ito et al. [24, 62, 63] introduced the generalized two-center cluster model (GTCM) where the valence neutrons are localized around one of the α -cluster cores and can be described as a single-particle motion in an atomic-like orbit. The representative results with GTCM were given for ^{10}Be and ^{12}Be . For example, the basis function for ^{10}Be can be defined as

$$\Psi_{m,n}^{J^\pi K}(S) = \mathcal{P}_K^{J^\pi} \cdot \mathcal{A} \{ \psi_L(\alpha) \psi_R(\alpha) \varphi(m) \varphi(n) \}_S, \tag{13}$$

where $\mathcal{P}_K^{J^\pi}$ is the projection operator with angular projection K , total spin projection J , and total parity projection π ; S is the relative distance parameter between two α -clusters; $\psi_L(\alpha)$ and $\psi_R(\alpha)$ represent the α -cluster wave function located at the left and right side, respectively; and $\varphi(m)$ and $\varphi(n)$ are the atomic orbits of the valence neutrons. The total wave function is finally given by taking a superposition over S and K as given below:

$$\Phi^{J^\pi} = \int dS \sum_{i,K} C_i^K(S) \Phi_i^{J^\pi K}(S), \tag{14}$$

where $C_i^K(S)$ is the coefficient which can be deduced from the GCM model:

$$0 = \int dS \sum_{i,K} C_i^K(S) \langle \Phi_i^{J^\pi K'}(S') | H - E^{J^\pi} | \Phi_i^{J^\pi K}(S) \rangle. \tag{15}$$

When the relative distance parameter S is fixed, the energy eigenvalue can be calculated by using Eq. (15).

GTCM describes the formation of the molecular orbits as well as the asymptotic cluster states depending on their relative distance [62], as shown in Fig. 1. In $S \geq 6 \text{ fm}$, the calculated energy surfaces and energies of the cluster-coupling wave function are almost uniform; however, in $S \leq 4 \text{ fm}$, the wave functions of the molecular orbits are expressed as a linear combination of various cluster-

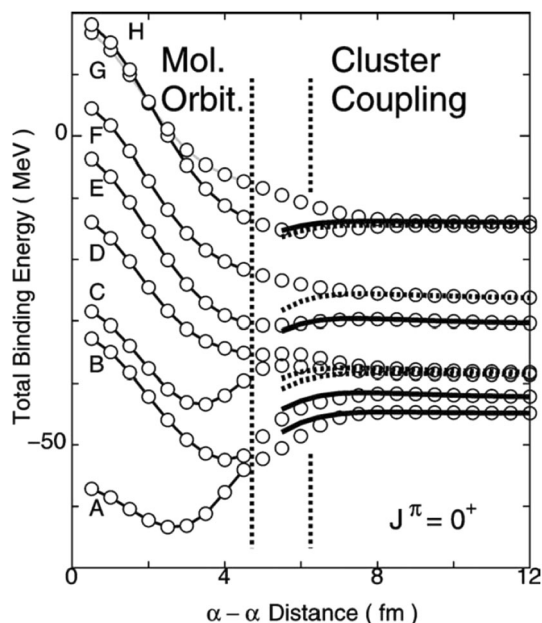


Fig. 1 Dynamical transition from the molecular orbits to the cluster-coupling states in the adiabatic energy surfaces. On the left side, the surfaces from A to H have a predominant molecular component for the valence neutrons of $(\pi_{3/2}^-)^2$, $(\sigma_{1/2}^+)^2$, $(\pi_{1/2}^-)^2$, $(\pi_{3/2}^+)^2$, $(\pi_{1/2}^+ \sigma_{1/2}^+)$, $(\pi_{1/2}^- \sigma_{1/2}^-)$, $(\sigma_{1/2}^-)^2$, and $(\pi_{1/2}^+)^2$, respectively. On the right side, the solid curves represent the energies of the $\alpha + {}^6\text{He}$ cluster states and the dotted curves show the energies of the ${}^5\text{He} + {}^5\text{He}$ cluster states. The figures are taken from Ref. [62]

coupling wave functions where the valence neutrons move around the alpha cores with a strong coupling configuration. The GTCM calculations also suggest the existence of $J^\pi = 6^+$ and $J^\pi = 7^-$ high spin states, which is in agreement with the measurements of Freer using two neutron transfer reactions ${}^{12}\text{C}({}^{12}\text{Be}, {}^{10}\text{Be}^* \rightarrow {}^4\text{He} + {}^6\text{He}) {}^{14}\text{C}$ [31].

A direct extension from ${}^{10}\text{Be}(\alpha + \alpha + 2n)$ to ${}^{12}\text{Be}(\alpha + \alpha + 4n)$ was conducted successfully about a decade ago [63], which developed a covalent super-deformation with a hybrid configuration of both the molecular-orbit and atomic-orbit configurations in the unbound region above the particle-decay thresholds of ${}^{12}\text{Be}$. Furthermore, after comparing the monopole transition strength of the GTCM with that of the single-particle model, Ito deduced that the total strength was comparable to or slightly larger than the single-particle strength which is considered to be one of the typical characteristics of the clustering structure of nuclei. This enhanced monopole transition strength was observed in Yang’s breakup-reaction experiment for ${}^{12}\text{Be}$ at RIBLL1 [26], the details of which are discussed in Sect. 3.

Ito also predicted, within the GTCM calculations [24, 25], that the 4^+ states with various cluster structures of ${}^4\text{He} + {}^8\text{He}$, ${}^6\text{He} + {}^6\text{He}$, and ${}^5\text{He} + {}^7\text{He}$ were located in

the energy region of 13.4–17.4 MeV. This coincides with the latest experimental observations of a broad (~ 1 MeV) $J^\pi = 4^+$ resonant state at the excitation energy of 14–15 MeV, presented by Freer et al. [64] in experiments using ${}^4\text{He}({}^8\text{He}, {}^4\text{He})$ and ${}^4\text{He}({}^8\text{He}, {}^6\text{He})$ reactions.

2.6 Antisymmetrized molecular dynamics

The antisymmetrized molecular dynamics model (AMD) is based on single-nucleon wave functions. As a consequence, this theoretical framework can represent not only the cluster structures but also the shell-model-like configurations [15].

The AMD wave function for the A -nucleon system is represented as a Slater determinant of single-nucleon Gaussian wave functions,

$$\Phi_{\text{AMD}}(\mathbf{Z}) = \frac{1}{\sqrt{A!}} \mathcal{A}\{\varphi_1, \varphi_2, \dots, \varphi_A\}, \tag{16}$$

where φ_i describes the single-particle wave function of the i th nucleon written as the product of spatial ($\phi_{\mathbf{Z}_i}$), intrinsic spin (χ_i) and isospin (τ_i) wave functions as follows:

$$\phi_{\mathbf{Z}_i}(\mathbf{r}_j) = \left(\frac{2v}{\pi}\right)^{4/3} \exp\left\{-v\left(\mathbf{r}_j - \frac{\mathbf{Z}_i}{\sqrt{v}}\right)^2\right\}, \tag{17}$$

$$\chi_i = \left(\frac{1}{2} + \xi_i\right)\chi_\uparrow + \left(\frac{1}{2} - \xi_i\right)\chi_\downarrow, \tag{18}$$

where \mathbf{Z}_i denotes the center of the Gaussian wave packet and ξ_i indicates the spin orientation. The width parameter v is fixed as a common and optimum value for the system under consideration. If all the Gaussian functions center around a common position, the AMD wave function in Eq. (16) will resemble the shell-model-like wave function. On the other hand, if all the Gaussian functions center around several positions, the AMD wave functions will produce the multi-cluster structures.

To obtain the expectation values of the observable operators such as the Hamiltonian and radii with energy variation [65], the AMD wave function should be projected to both the parity and angular-momentum eigenstates. In the conventional AMD calculation, the energy variation is done after the parity projection (VAP) and before the angular-momentum projection (VBP) [66]. The parity-projected wave function can be expressed as

$$\Phi^\pm(\mathbf{Z}) \equiv \mathcal{P}^\pm \Phi_{\text{AMD}}(\mathbf{Z}) = \frac{1 \pm \mathcal{P}_r}{2} \Phi_{\text{AMD}}(\mathbf{Z}), \tag{19}$$

where $\mathcal{P}^\pm = (1 \pm \mathcal{P}_r)/2$ denotes the parity projection operator. Using the good-spin wave function $\Phi^\pm(\mathbf{Z})$, the angular-momentum projected wave function can be defined as

$$\Phi_{MK}^{J^\pm}(\mathbf{Z}) = \int d\Omega D_{MK}^{J^*}(\Omega) \mathcal{R}(\Omega) \Phi^\pm(\mathbf{Z}), \tag{20}$$

where $\mathcal{P}_{MK}^J \equiv \int d\Omega D_{MK}^{J^*}(\Omega) \mathcal{R}(\Omega)$ is the total angular-momentum projection operator. Its expectation values are numerically calculated by a summation over the mesh points of the Euler angles Ω , where $\mathcal{R}(\Omega)$ represents the rotation operator and $D_{MK}^{J^*}(\Omega)$ is the Wigner's D-function. The correct K quantum number for each spin parity can be deduced from the principle that the energy expectation value for the spin parity eigenstate $\Phi_{MK}^{J^\pm}(\mathbf{Z})$ is a minimum [34].

The wave function $\Phi(\mathbf{Z}_1^{J^\pm})$ of the lowest J_1^\pm state, which can be expressed as $\Phi_{MK}^{J^\pm}(\mathbf{Z}_1^{J^\pm})$, is calculated by varying the parameters \mathbf{Z}_i and ξ_i in Eqs. (17) and (18), in order to obtain the smallest expectation values of the Hamiltonian [67]. The wave functions $\Phi(\mathbf{Z}_n^{J^\pm})$ are superposed to be orthogonal to the lower states as given in Eq. (21) [68, 69]:

$$\Phi_{MK}^{J^\pm}(\mathbf{Z}_n^{J^\pm}) = \sum_{k=1}^{n-1} \frac{\langle \Phi(\mathbf{Z}_k^{J^\pm}) | \Phi(\mathbf{Z}_n^{J^\pm}) \rangle}{\langle \Phi(\mathbf{Z}_k^{J^\pm}) | \Phi(\mathbf{Z}_k^{J^\pm}) \rangle} \Phi(\mathbf{Z}_k^{J^\pm}). \tag{21}$$

The final results are constructed by diagonalizing the Hamiltonian matrix $\langle \Phi(\mathbf{Z}_i^{J^\pm}) | H | \Phi(\mathbf{Z}_j^{J^\pm}) \rangle$ formed from all the involved intrinsic states.

Kanada-En'yo explored the structure of the excited states of ^{10}Be by the method of VAP in the basic framework of AMD [68]. The density distribution of the intrinsic wave functions for the band-head states of ^{10}Be was determined as shown in Fig. 2, wherein a well-developed

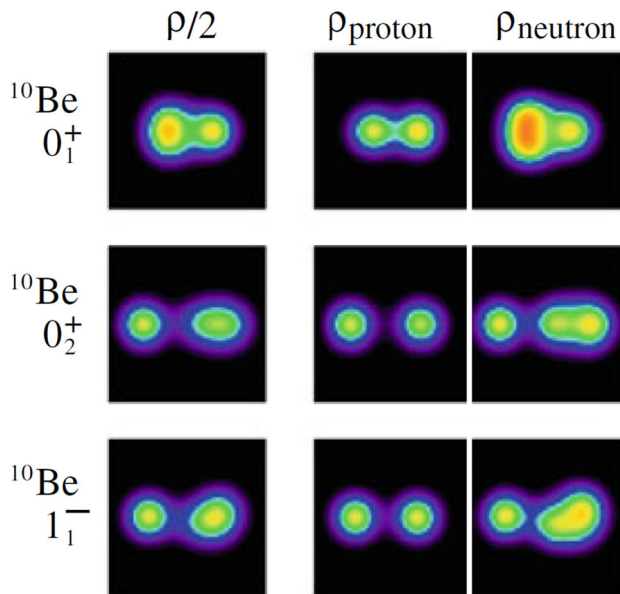


Fig. 2 (Color online) Density distribution of the intrinsic wave functions for the band-head states of ^{10}Be . The distributions for matter, proton, and neutron densities are illustrated in the left, middle and right panels. The figures are taken from Ref. [70]

2α cluster configuration surrounded by the valence neutrons can be seen.

In order to understand the motion of the valence neutrons around the core clusters, the single-particle wave functions should be determined from the traditional AMD wave function [71]. As the single-particle wave functions φ_i in Eq. (16) are not orthonormal, another base wave function $\tilde{\varphi}_\alpha$ must be constructed as follows:

$$\tilde{\varphi}_\alpha = \frac{1}{\sqrt{\lambda_\alpha}} \sum_{i=1}^A c_{i\alpha} \varphi_i, \tag{22}$$

where λ_α and $c_{i\alpha}$ are the eigenvalues and eigenvectors of the overlap matrix $B_{ij} \equiv \langle \varphi_i | \varphi_j \rangle$. Thus, the single-particle Hamiltonian can be calculated and diagonalized for the Hamiltonian operator as $H \equiv \sum_i \hat{t}_i + \sum_{i < j} \hat{V}_{ij} + \sum_{i < j < k} \hat{V}_{ijk}$, which is a sum of three terms, namely the kinetic term, two-body interaction term and three-body interaction term, respectively. As a result, the AMD-HF single-particle energies, parity components as well as the angular momenta can be calculated.

The AMD program was extended to deal with the 3α -cluster structures in the neutron-rich carbon isotopes by Baba and Kimura [41, 42, 72, 73]. With the help of the AMD-HF method, Baba determined the single-particle wave functions of the valence neutrons, leading to the explicit identification of the so-called π -bond or σ -bond molecular configurations. For ^{14}C , three different clustering structures with distinct magnitudes of deformation and various valence neutron configurations, namely the triangular, π -bond linear chain and σ -bond linear-chain configurations, were exhibited as shown in Fig. 3. The calculated energies and α reduced widths of the π -bond linear-chain state are close to the resonances observed in the $^4\text{He} + ^{10}\text{Be}$ scattering experiments [36, 74].

Furthermore, an analysis of the decay patterns by Baba suggests that the σ -bond linear-chain state decays almost exclusively to the ~ 6 MeV states in ^{10}Be , whereas the other resonant states decay mostly to the first excited state (3.4 MeV, 2^+) as well as the ground state in ^{10}Be . This decay pattern is considered to be a strong characteristic of the σ -bond linear-chain formation, which is consistent with the experimental observations of Li et al. at CIAE [38].

For ^{16}C , the AMD calculations show the existence of both the triangular and linear-chain configurations [72]. The energy spectrum of ^{16}C reconstructed from the $^6\text{He} + ^{10}\text{Be}$ breakup reaction [43] shows a rough peak at about 20.6 MeV, which was interpreted as a possibility for a linear-chain configuration. The need for further experimental investigation of the various cluster states in ^{16}C is imperative.

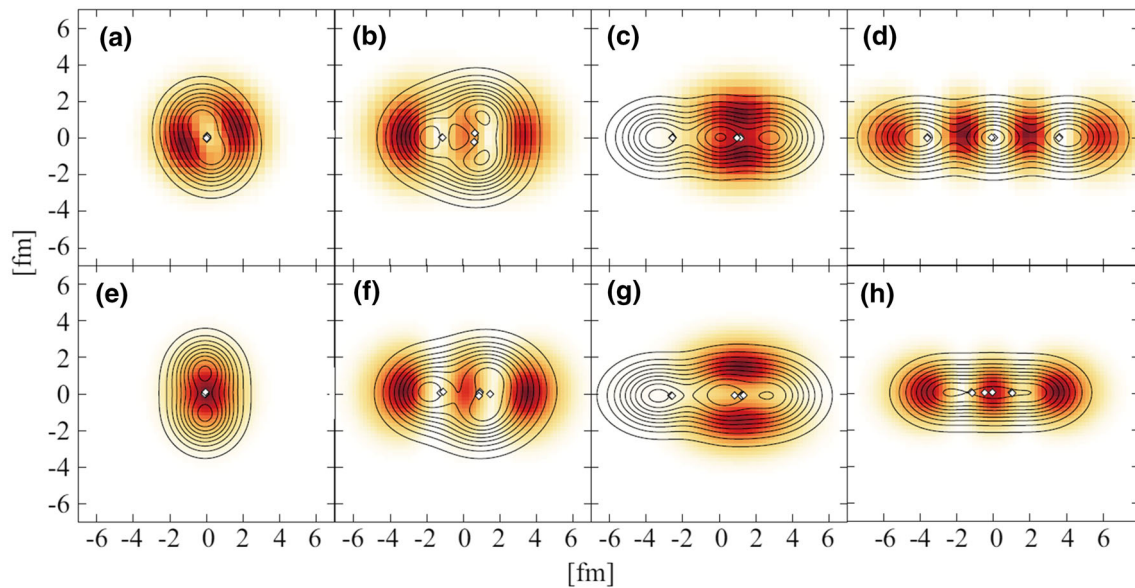


Fig. 3 (Color online) Density distribution of the positive (a–d) and negative parity states (e–h) of ^{14}C . a, e, and h represent non-cluster structures; b and f display the triangular configurations; c and g show the π -bond linear-chain configurations, and d exhibits the σ -bond linear-chain configuration. The contour lines show the proton density

Recently, Arumugam et al. [75] developed the RMF approach to investigate the clustering phenomena in light-mass stable and uncommon nuclei. The RMF calculations of the spatial distribution of the nuclear density and deformation parameters show the existence of α -clustering and halo structures. However, the limitations of the RMF method are evident as it adopts the oscillator basis, which is improper for large deformations and weak binding. The space reflection symmetry of the RMF method places further restrictions on describing a nucleus with an asymmetric form, e.g., triaxial shapes.

3 Experimental developments

In spite of the significant progress made in the theoretical description of the cluster structures as outlined above, only a few cluster states have been confirmed by experiments so far, as many physical quantities of the nuclei in question must be determined simultaneously to accurately identify the cluster structures, which is a great challenge for experimentalists [22, 26, 30, 33].

The following four criteria are often required to identify a particular cluster (molecular) structure with certainty: [26, 38]: (1) A clear determination of the excitation energy versus spin–parity systematics related to a specific rotational band with a distinctively large moment of inertia. (2) A large cluster (such as alpha) decay width. (3) An enhanced characteristic transition (such as the monopole

distributions. The colored plots show the single-particle orbits occupied by the most weakly bound neutron. The open boxes show the centroids of the Gaussian wave packets describing the protons. The figures are taken from Ref. [41]

transition) strength. (4) A selective decay path corresponding to a cluster structural link. Both the invariant mass method (IM) and missing mass method (MM) are crucial to determine these physical quantities.

In addition to the high-energy knockout reaction used for investigating the ground state structure and the fusion evaporation reaction used for exploring the very high-lying cluster states near the $N\alpha$ breakup thresholds [76], there are three major types of reaction methods which have been extensively used in the previous experiments to study the cluster structures in excited states near the corresponding cluster decay thresholds. These are the inelastic excitation and decay (sometimes called elastic breakup) reactions [26, 31, 39, 40, 43, 77], transfer reactions [29, 37, 38, 78], and resonant scattering reactions [36, 64, 74]. These tools need to be selected carefully in order to populate some specific cluster states.

For the breakup reactions, Takemoto suggested, within the framework of the AMD method, that the optimum incident energy range is approximately 20–30 MeV/nucleon [79] for cluster studies. If the incident energy is larger than 50 MeV/nucleon, the cluster structures inside the incident particles would mostly be destroyed during the breakup process.

For the transfer reactions, it is better to use mass combinations associated with the large Q value. This would help in selecting the reaction channel and populating the high-lying excited cluster states [37]. For example, Li et al. chose the $^9\text{Be} (^9\text{Be}, ^{14}\text{C}^* \rightarrow ^4\text{He} + ^{10}\text{Be}) ^4\text{He}$ with Q -

value as large as 17.3 MeV, to study the decay paths of the highly excited states, above 20 MeV, in ^{14}C [38], which are difficult to investigate with other reaction mechanisms.

Moreover, the structure link between the parent and daughter nucleus in the decay scheme is another important clue for the selective investigation of cluster structures. The parent nucleus has a large possibility of decaying to the final state of the daughter nucleus, which possesses a similar structure configuration. This structural link in the decay scheme has been verified both experimentally and theoretically [38, 41].

3.1 Inelastic excitation and decay

In order to explore the cluster structures in ^{12}Be , Yang et al. carried out a breakup reaction using a 29 MeV/nucleon ^{12}Be secondary beam with an approximate intensity of 3000 pps, off a carbon target [26, 27]. The detection was concentrated at most forward angles by using a zero-degree telescope. Owing to the well-developed self-calibration methods for the double-sided silicon detectors (DSSD) [80], the energy resolutions were good enough to get an unambiguous particle identification of the breakup fragments ^4He , ^6He , and ^8He . Two helium fragments in coincidence can, therefore, be clearly selected. As a consequence, the excitation energy spectra for ^{12}Be can be reconstructed with the $^6\text{He} + ^6\text{He}$ and $^4\text{He} + ^8\text{He}$ decay channels, as shown in Fig. 4.

For the $^6\text{He} + ^6\text{He}$ decay channel, two peaks at 11.7 MeV and 13.3 MeV are clearly observed whose respective spin-parity, 2^+ and 4^+ , was verified with the distorted wave Born approximation (DWBA) calculation. The events near the corresponding decay threshold of

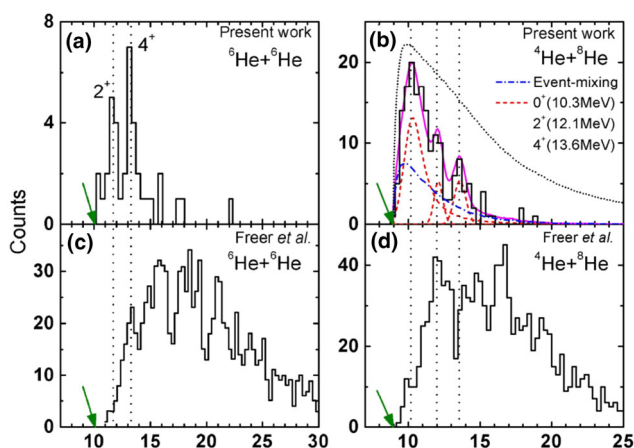


Fig. 4 (Color online) Excitation energy spectra of ^{12}Be reconstructed with the **a** $^6\text{He} + ^6\text{He}$ and **b** $^4\text{He} + ^8\text{He}$ decay channels, compared with those reported in Ref. [31], (c, d). The green arrows show the respective cluster decay thresholds. The figures are taken from Ref. [26]

10.1 MeV can be expressed as the potential 0^+ band-head state, which needs more concrete observation. For the $^4\text{He} + ^8\text{He}$ decay channel, three peaks at about 10.3 MeV, 12.1 MeV, and 13.6 MeV are identified. The spin-parities of the first and last states are assigned to 0^+ and 4^+ , respectively, with the model-independent angular correlation analysis [30], which are in good agreement with the GTCM calculations [25]. Due to the low statistics, the spin-parity of the 12.1 MeV state is only tentatively assigned to 2^+ , according to the GTCM predictions. These observed states, except for the new 11.7 MeV and 10.3 MeV states, agree quite well with those reported by Freer [26] and Charity [81]. The molecular rotational bands can then be constructed from these experimental measurements, as shown in Fig. 5, whose $\hbar^2/2\mathfrak{I}$ values are approximately 0.15 MeV. The large value of the moment of inertia \mathfrak{I} is closely linked to the strongly deformed structure, which is a characteristic evidence for the cluster formation in ^{12}Be , as indicated by the clustering criterion 1.

From a least-square fitting of the observed spectrum with the Breit-Wigner line shape function with angular momentum $L = 0$ [82], the total decay width of the 10.3 MeV excited state in ^{12}Be is deduced to be $\Gamma_{\text{tot}} = 1.5(2)$ MeV, in conformance with the predictions of a particularly large width for a cluster band head just above the threshold [69]. The dominating decay channels for this resonant state are the binary helium cluster channels and the neutron or γ emission, which can be written as $\Gamma_{\text{tot}} \approx \Gamma_{\text{He}} + \Gamma_{\text{Be}}$. The beryllium branch ratio is taken as $\Gamma_{\text{Be}}/\Gamma_{\text{tot}} = 0.28(12)$ from Korshennikov's measurements [83]. Therefore, the helium branch ratio can be deduced as $\Gamma_{\text{He}}/\Gamma_{\text{tot}} = 0.72(12)$ and the partial cluster decay width is $\Gamma_{\text{He}} = 1.1(2)$ MeV. Based on the single-channel R-matrix approach [84], the reduced decay width

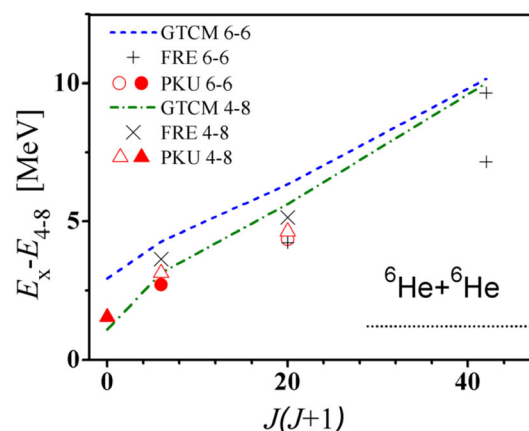


Fig. 5 (Color online) Energy-spin systematics for the resonant states in ^{12}Be associated with the $^6\text{He} + ^6\text{He}$ and $^4\text{He} + ^8\text{He}$ configurations. The vertical axis is defined with respect to the separation energy of the $^4\text{He} + ^8\text{He}$ channel. The figures are taken from Ref. [27]

is $\gamma_{\text{He}}^2 = 0.50(9)$ MeV and the dimensionless cluster spectroscopic factor can be expressed as $\theta_{\text{He}}^2 = 0.53(10)$ [28]. This is comparable to that for typical clustering states such as the 4^+ state in ^{10}Be ($\theta_{\text{He}}^2 = 0.66-2.23$) [85], providing a strong affirmation for the clustering structure in ^{12}Be , as indicated by the clustering criterion 2.

The isoscalar monopole transition strength $M(\text{IS}, 0)$ can be deduced from the multipole-decomposition analysis of the inelastic scattering cross section [86]. As shown in Fig. 6, the distorted wave Born approximation (DWBA) calculations ($\frac{d\sigma}{d\Omega}_{L=0, \text{DWBA}}$, with a normalization factor of $a_0 = 0.034(10)$, are perfectly consistent with the experimental differential cross sections ($\frac{d\sigma}{d\Omega}_{\text{exp}}$). The factor a_0 can be corrected as $0.075(24)$ considering the 0^+ state (10.3 MeV) in the entire excitation spectrum. The energy-weighted sum rule (EWSR) for isoscalar transitions can be written as [87]

$$\text{EWSR}(\text{IS}, 0) \cdot a_0 = |M(\text{IS}, 0)|^2 \cdot E_0 = \frac{2\hbar^2}{m} A R_{\text{rms}}^2, \quad (23)$$

where m is the nucleon mass, A is the nuclear mass number, and R_{rms} is the root-mean-square matter radius of the nucleus. With Eq. (23), $M(\text{IS}, 0)$ can be deduced as $7.0 \pm 1.0 \text{ fm}^2$, which is comparable to the typical clustering states such as the Hoyle state in ^{12}C ($5.4 \pm 0.2 \text{ fm}^2$) [60] and in accordance with the GTCM calculations. It gives a strong confirmation of the clustering structure in ^{12}Be as mentioned in the clustering criterion 3.

In conclusion, a distinct clustering structure is justified for the 10.3 MeV (0^+) state in ^{12}Be , based on the three clustering criteria outlined above.

In view of the considerable success in identifying the cluster states in neutron-rich beryllium nuclei, it is reasonable to extend the clustering investigations to neutron-

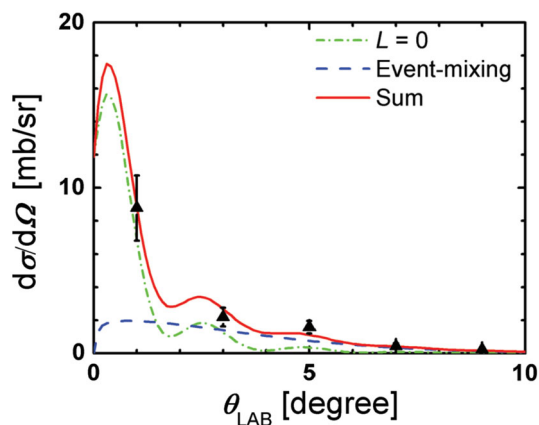


Fig. 6 (Color online) Experimental differential cross sections compared with the DWBA calculations for the 10.3 MeV state in ^{12}Be . The figures are taken from Ref. [27]

rich carbon isotopes and oxygen isotopes. Feng et al. conducted a breakup reaction using a 65 MeV ^{13}C primary beam onto a self-supporting ^9Be target [40]. The purpose was to determine the spin-parity and isoscalar monopole transition strength of the 14.3 MeV resonant state in ^{13}C .

The experimental and calculated differential cross sections with the FRESKO code [88] for the 14.3 MeV state in ^{13}C are shown in Fig. 7. It is obvious that only the calculation with $J^\pi = (1/2)^-$ generates the oscillatory character of the experimental results, whereas the $J^\pi = (5/2)^-$ and $J^\pi = (7/2)^-$ configurations do not agree with the observations. As a result, the spin-parity of the 14.3 MeV resonant state in ^{13}C can be assigned to $J^\pi = (1/2)^-$, in agreement with the $(1/2)_5^-$ state in ^{13}C as predicted by the OCM calculations [59]. The isoscalar monopole transition strength $M(\text{IS}, 0)$ of this resonant state can be determined by following the same procedure as applied for ^{12}Be . The resulting value is $6.3 \pm 0.6 \text{ fm}^2$, even larger than the theoretical prediction of 3.3 fm^2 within the OCM approach. This enhanced monopole transition strength is an indication of the cluster structure in ^{13}C , according to the clustering criterion 3.

With an objective of investigating the near-threshold cluster resonance in ^{14}C , Zang et al. conducted a breakup reaction using a 25.3 MeV/nucleon ^{14}C secondary beam with an approximate intensity of 2×10^4 pps, off a CH_2 target [39]. By gating on the Q_{ggg} peak at about -12.0 MeV for ^{10}Be on the ground state, the resonant states of ^{14}C can be reconstructed with the $^4\text{He} + ^{10}\text{Be}(\text{g.s.})$ decay channel, as shown in Fig. 8, together with the previous observations of Freer [77].

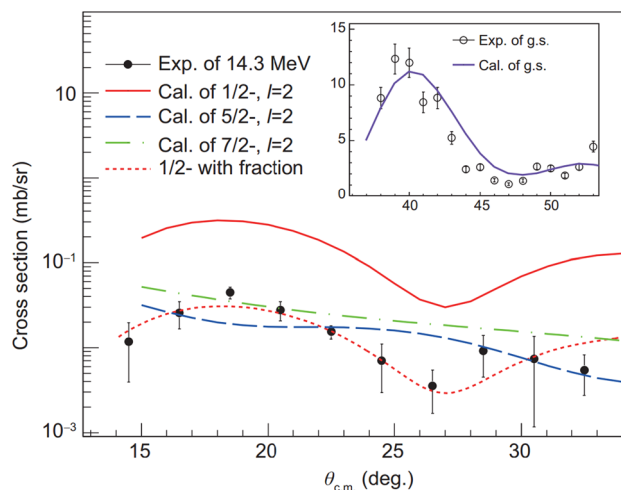


Fig. 7 (Color online) Experimental and calculated differential cross sections with FRESKO code within the CDCC framework for the 14.3 MeV state in ^{13}C . The figures are taken from Ref. [40]

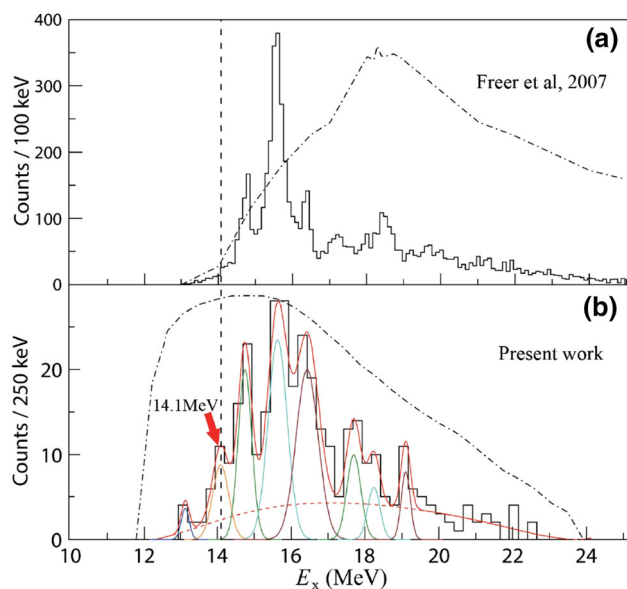


Fig. 8 (Color online) Resonant states of ^{14}C deduced from the $^4\text{He} + ^{10}\text{Be}(\text{g.s.})$ decay channel, measured in the **a** previous and in the **b** present experiments. The figures are taken from Ref. [39]

In Fig. 8, the resonant states at 14.8 MeV and 15.6 MeV are distinctly identified in the previous and present measurements, whose spin-parities are assigned to 5^- and 3^- , respectively. Due to the low statistics of another clearly observed 14.1 MeV peak, it is difficult to determine the spin-parity information by the angular correlation or differential cross-sectional methods. However, by comparing the observed relative yields between 14.1 and 15.6 MeV states, the spin of the 14.1 MeV resonant state is constrained to be 0, 1, and 2. This is compatible with the prediction of a 0^+ band head at about 14 MeV for a π -bond linear-chain configuration [73]. It would be interesting to study this state further with a direct determination of its spin and cluster decay branching ratio.

3.2 Transfer reactions

Transfer reactions are also considered to be an important approach to explore the cluster structures in neutron-rich light nuclei. For example, Jiang et al. performed an experiment using a 45 MeV ^9Be primary beam with an approximate intensity of 7 nA, off a self-supporting ^9Be target [29] to study the high-lying excited states in ^{10}Be . The $\alpha + ^6\text{He}$ and $t + ^7\text{Li}$ decay channels were detected simultaneously by the invariant mass as well as missing mass methods.

The experimental Q -value spectrum of three different decay channels, namely $^9\text{Be} (^9\text{Be}, ^8\text{Be} \rightarrow \alpha + \alpha)$, $^9\text{Be} (^9\text{Be}, ^{10}\text{Be}^* \rightarrow \alpha + ^6\text{He})$, and $^9\text{Be} (^9\text{Be}, ^{10}\text{Be}^* \rightarrow t + ^7\text{Li})$, is shown in Fig. 9, by selecting the coincidence

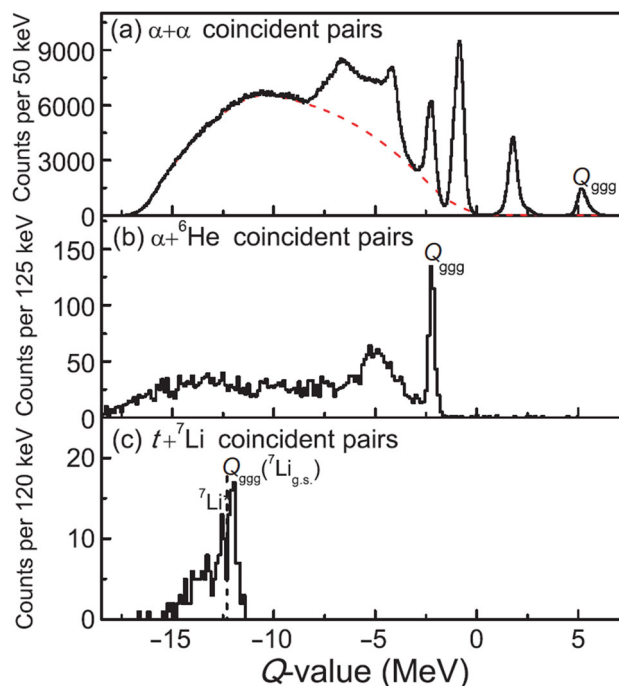


Fig. 9 Experimental Q -value spectrum for 3 coincident events: **a** $^9\text{Be} (^9\text{Be}, ^8\text{Be} \rightarrow \alpha + \alpha)$, **b** $^9\text{Be} (^9\text{Be}, ^{10}\text{Be}^* \rightarrow \alpha + ^6\text{He})$, and **c** $^9\text{Be} (^9\text{Be}, ^{10}\text{Be}^* \rightarrow t + ^7\text{Li})$. The figures are taken from Ref. [29]

events in detectors. The missing mass spectrum for ^{10}Be can be extracted by gating on the Q -value peaks in Fig. 9a. Owing to the appropriate energy calibration and event selection, the four measured excited states as well as the ground state are consistent with the previous observations [89].

By gating on the peaks in Fig. 9b, the energy spectrum for ^{10}Be can be obtained from $\alpha + ^6\text{He}$ coincident events by the standard invariant mass method, where a new state is located at 15.6 MeV in agreement with the proposed 6^- member of the 1^- (5.96 MeV) rotational band [90].

By gating on the peaks in Fig. 9c, the energy spectrum for ^{10}Be can be reconstructed from $t + ^7\text{Li}$ coincident events in a similar manner. The 18.55 MeV excited state is found to decay to the ground state of ^7Li as well as the 0.478 MeV state with a relative branch ratio of 0.93 ± 0.33 and the 18.15 MeV excited state decays predominately to the ground state of ^7Li , which is inconsistent with the previous experimental result [32]. This abnormal decay pattern of the high-lying excited states in ^{10}Be may indicate some unique cluster structures that require further theoretical investigations.

The clustering investigations with transfer reactions were extended to the neutron-excess carbon isotopes as well. For example, Li et al. recently succeeded in searching for promising evidence of the intriguing σ -bond linear-

chain structure in ^{14}C from the transfer reaction $^9\text{Be} (^9\text{Be}, ^{14}\text{C}^* \rightarrow ^4\text{He} + ^{10}\text{Be}) ^4\text{He}$ with $Q = 17.3$ MeV [38]. The experimental Q -value spectra with a very clean Q_{ggg} peak and two additional clean peaks are shown in Fig. 10, which makes it possible to clearly select the final states of ^{10}Be fragments.

By gating on different Q -value peaks in Fig. 10, the excitation spectra of ^{14}C can be obtained from the $\alpha + ^{10}\text{Be}$ fragments by the invariant mass method. The excited states located at 16.5 MeV, 19.8 MeV, 20.8 MeV, 21.4 MeV, and 22.5 MeV agree quite well with the previous experimental results [91]; moreover, a new resonant state at 23.5(1) MeV is clearly identified which decays dominantly to the first excited state in ^{10}Be and must be further investigated.

The relative branching ratio of the 22.5(3) MeV resonant state in ^{14}C has been quantitatively determined as shown in Fig. 11. This state is found to decay strongly to the ~ 6 MeV states in ^{10}Be , which corresponds well with the band head at 22.2 MeV of the σ -bond linear-chain molecular band within the framework of AMD, as predicted by Baba [41].

The theoretical predictions suggest a pure decay branching ratio to the ~ 6 MeV states, whereas the experimental observations show a small fraction of the branching ratio to the ground state and the first excited state in ^{10}Be , as illustrated in Fig. 11. This may be inferred as the existence of other configurations, except for the σ -bond linear-chain structure in the 22.5(3) MeV state. Out of the four contiguous states in the ~ 6 MeV region, namely 5.958 MeV(2^+), 5.96 MeV(1^-), 6.18 MeV(0^+), and 6.26 MeV(2^-), only the 6.18 MeV(0^+) state has a pure σ -bond configuration, whereas the other three states possess a π -bond configuration [22]. Therefore, it can be presumed

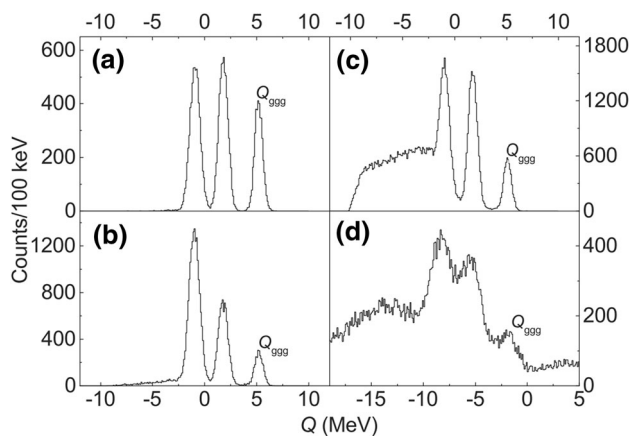


Fig. 10 Experimental Q -value spectrum for three data sets: **a** identified ^{10}Be and identified α , **b** identified ^{10}Be and unidentified α , and **c** identified α and unidentified ^{10}Be . Spectrum **d** is taken from a previous experiment [91]. The figures are taken from Ref. [38]

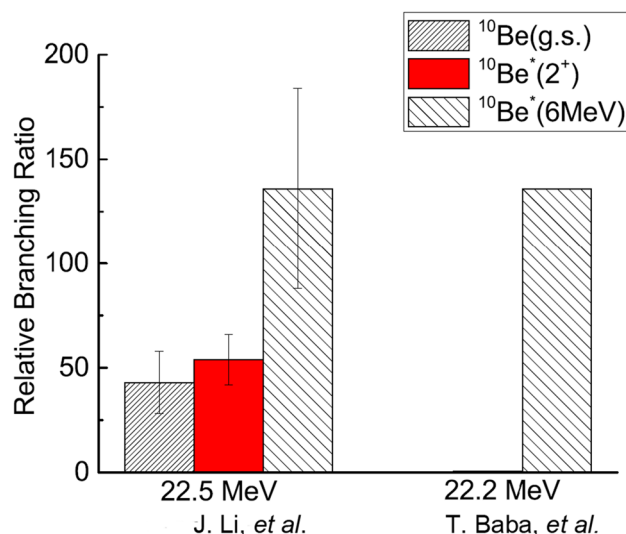


Fig. 11 (Color online) Comparison of the relative decay branching ratio obtained from the experiment [38] from the theoretical prediction [41]

that the predominantly collected final state in ^{10}Be should be the 6.18 MeV state with spin-parity $J^\pi = 0^+$. This special structural link between the parent and daughter nucleus is another important clustering criterion (4) as shown qualitatively in Fig. 12.

3.3 Resonant scattering reactions

Resonant scattering with projectiles traveling through a light thick target was studied by several groups to investigate the nuclear clustering in some resonant states. The targets are required to be thick enough to stop the beam projectiles so that the detectors can be placed at zero degrees, covering the large backward angles in the c.m. frame [92]. As the beam particles slowdown in the target, a resonant state may be created inside the projectile-target composite system when the c.m. energy coincides with the corresponding resonant energy. The excited composite system subsequently decays into the projectile and target nuclei. In general, the beam particles should be heavier than the target nucleus, in order to apply detection in inverse kinematics. As different resonances would be produced at different positions within the target, corrections must be made for the detection solid angle for each resonance. In addition, the effects of inelastic scattering must be taken into account, which may lead to false identification of a resonant energy.

Freer et al. [85] reported a resonant $^6\text{He} + ^4\text{He}$ scattering experiment to investigate the molecular clustering structure in the resonances of ^{10}Be . When the c.m. energy, contributed by the energy of the ^6He projectile, is equal to a certain resonance-energy of ^{10}Be , a composite nucleus is

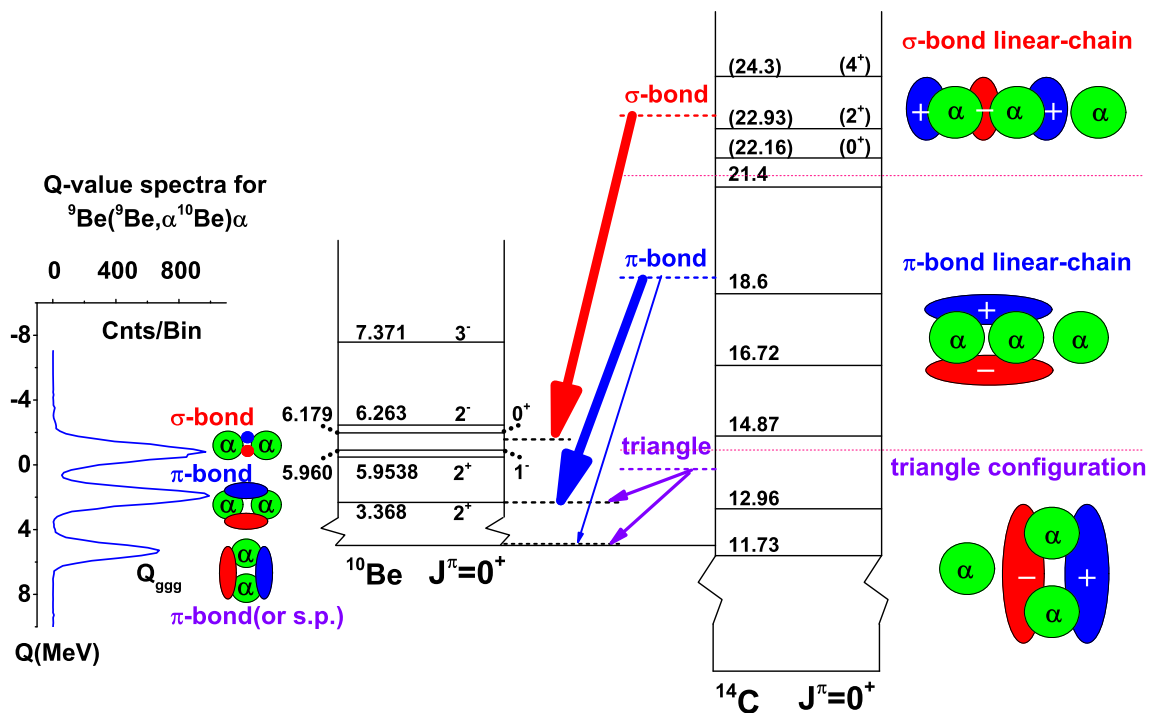


Fig. 12 (Color online) Selective decay patterns of high-lying excited states of ${}^{14}\text{C}$ due to the structural link

produced which subsequently decays into the fragments ${}^6\text{He} + {}^4\text{He}$. These fragments can be coincidentally observed by suitably placed detectors.

The angular distribution of the c.m. for the 10.15 MeV resonance was experimentally determined as shown in Fig. 13. The simulation results with a single Breit–Wigner formula demonstrate that the oscillatory behavior of the

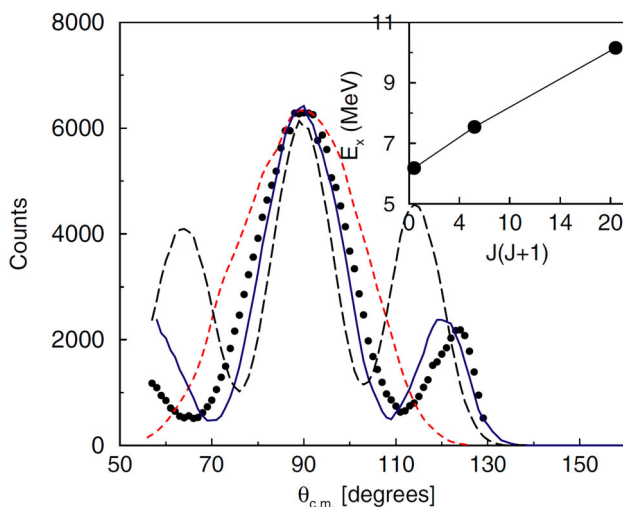


Fig. 13 (Color online) Experimentally determined c.m. distribution (data points), compared with simulations for the decay of a resonance with spin 4 (blue solid line), 2 (red-dashed line), and 6 (black long-dashed line). The inset shows the energy-spin systematics of the rotational band, of which the present 4^+ state is a member. The figures are taken from Ref. [85]

experimental angular distribution can only be reproduced with a spin–parity of $J^\pi = 4^+$, which is considered as the third member of a rotational band with a 6.18 MeV(0_2^+) band head state. The $\hbar^2/2\mathcal{I}$ value of this rotational band is about 0.20 MeV, which is comparable with that of the 10.3 MeV(0^+) rotational band in ${}^{12}\text{Be}$, suggesting a large deformation in the 10.15 MeV resonant state [26]. Moreover, the alpha decay width (Γ_α) was deduced to be 0.10–0.13 MeV from the measured distributions and the branching ratio was $\Gamma_\alpha/\Gamma_{\text{tot}} = 0.35$ –0.46. The corresponding dimensionless cluster spectroscopic factor ($\theta_\alpha^2 = 0.66$ –2.23), which is comparable to that of the 10.3 MeV(0^+) cluster resonance in ${}^{12}\text{Be}$. Such a large deformation of the rotational band and large alpha decay width confirm a well-developed $\alpha : 2n : \alpha$ molecular structure in ${}^{10}\text{Be}$.

Similar methods were developed by several groups to study the cluster structures in neutron-rich ${}^{14}\text{C}$. Freer et al. performed another resonant scattering reaction with ${}^{10}\text{Be}$ and ${}^4\text{He}$ to obtain the resonant spectra [36]. The associated spin–parity information was discussed in detail with an analysis of the angular distribution. Monte Carlo simulations were applied to determine the energy loss processes of the decay fragments and the solid angle associated with the interaction position in the thick target. The experimental angular distribution for the 18.8 MeV resonance was compared with that of the simulation results, as illustrated in Fig. 14. It can be seen that the experimental

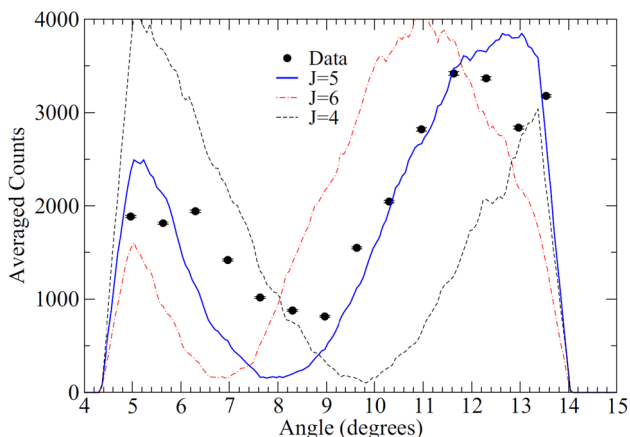


Fig. 14 (Color online) The experimental angular distributions for 18.8 MeV resonance at 32 MeV beam energy are compared with that of the simulations with $J^\pi = 4^+, 5^-, 6^+$. The figures are taken from Ref. [36]

data are in agreement with a spin-parity of $J^\pi = 5^-$. Similar angular distribution analysis was extended to the high-lying 17.2 MeV and 20.9 MeV resonances as well, whose spin-parity is proposed to be $J^\pi = 3^-$ and $J^\pi = 6^+$, respectively.

The experimental excitation function above 16.5 MeV can be analyzed by the R -matrix method [84] and the resonance parameters such as the resonant energy, spin-parity and α -decay widths can be determined. The R -matrix analysis proposes that these resonant states have large α -decay widths which are close to the Wigner limit, indicating a strongly deformed $^{10}\text{Be} + ^4\text{He}$ cluster structure in ^{14}C .

In order to collect more evidence for the cluster configurations in ^{14}C , Fritsch et al. carried out further $^{10}\text{Be} + ^4\text{He}$ resonant scattering experiments with the newly developed AT-TPC detector [93], which covers a larger range of c.m. angles for both elastic and inelastic scattering measurements [74]. Figure 15 shows the

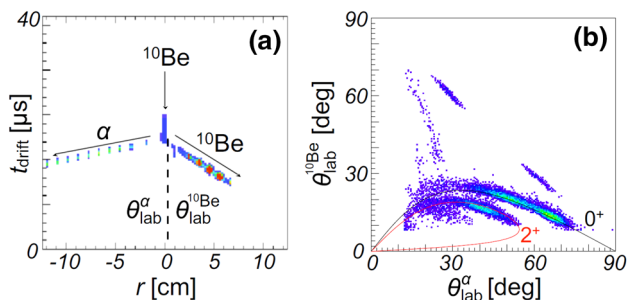


Fig. 15 (Color online) The trajectories of a $^{10}\text{Be} + ^4\text{He}$ resonant scattering event and the kinematical correlation of the θ_{lab} between ^{10}Be and ^4He . The figures are taken from Ref. [74]

trajectories of the $^{10}\text{Be} + ^4\text{He}$ resonant scattering event and the kinematical correlation of the θ_{lab} between ^{10}Be and ^4He . The resonance parameters can be obtained by the R -matrix method. Two resonances in ^{14}C located at 15.0 MeV and 19.0 MeV were assigned a spin-parity of 2^+ and 4^+ , and a spectroscopic factor of 30% and 20%, respectively.

It is worth noting that a recent $^{10}\text{Be} + ^4\text{He}$ resonant scattering experiment was reported by Yamaguchi et al. [94], in which the rotational band with a linear-chain configuration in ^{14}C was suggested. The elastic scattering excitation function in this experiment is illustrated in Fig. 16. R -matrix calculations with a single channel involved were performed to determine the resonance parameters.

Based on the AMD calculation, Suhara and Kanada-En'yo proposed a prolate band ($J^\pi = 0^+, 2^+, 4^+$) with a linear-chain cluster structure at a few MeV about the $^{10}\text{Be} + ^4\text{He}$ threshold [95]. By the angular distribution and R -matrix analyses, spin-parities of $0^+, 2^+$, and 4^+ were assigned to the three resonances located at 15.1 MeV, 16.2 MeV, and 18.7 MeV, respectively, which are in excellent agreement with the predictions. By fitting the energy-spin systematics, the newly identified resonances can be interpreted as a rotational band, whose $\hbar^2/2\mathcal{I}$ value is approximately 0.19 MeV, indicating a strongly deformed structure in conformance with the linear-chain configuration.

Many experiments have been conducted with the resonant scattering method to investigate the clustering structure in ^{14}C up to now. However, there is no consistency in these results, which indicates that more measurements using different methods are necessary.

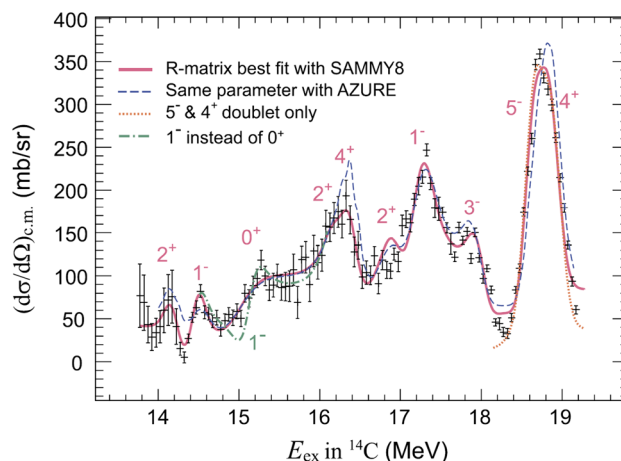


Fig. 16 (Color online) Elastic scattering excitation function fitted with R -matrix method. The figures are taken from Ref. [94]

4 Summary

Nuclear clustering is one of the most fundamental aspects of nuclear structure. A number of theoretical models have been developed to describe the cluster phenomena inside a nucleus, which are outlined in Sect. 2. The predictions include various clustering configurations, such as the triangle form, linear-chain states, and alpha condensation states. Many significant properties of the cluster states, including the excitation energy, spin–parity, cluster decay width, characteristic transition strength, and specific decay patterns, can be determined from these theoretical calculations.

Various experimental tools, such as the inelastic excitation and decay (breakup reaction), transfer reactions, and resonant scattering reactions have been employed to investigate cluster structures inside the nucleus. For the breakup reaction, the optimum incident energy is approximately 20–30 MeV/nucleon. For the transfer reactions, the reaction channel with a large Q value is favorable for separating the decay paths and populating the high-lying states. For the resonant scattering reactions, the resonance parameters can be determined from the angular distribution analysis and R -matrix calculations. Cluster states are believed to reside in a rotational band with large moments of inertia and possess large cluster decay widths. Characteristic transition strength or selective decay patterns are also used as criteria for identifying a cluster state.

Despite the noteworthy progress made in the past, many open questions remain in the study of clustering phenomena in neutron-rich light nuclei. Considering the linear-chain configuration as an example, theoretical calculations have predicted the existence of linear-chain structures in ^{14}C and ^{16}C . However, experimental evidence is still very limited. The use of some novel detectors, such as AT-TPC [93] and very thin double-sided silicon strip detectors [96] should be of great help in future experimental investigations.

References

1. J.A. Peacock, S. Cole, P. Norberg et al., A measurement of the cosmological mass density from clustering in the 2dF Galaxy Redshift Survey. *Nature* **410**, 169 (2001). <https://doi.org/10.1038/35065528>
2. H.X. Chen, W. Chen, X. Liu et al., The hidden-charm pentaquark and tetraquark states. *Phys. Rep.* **639**, 1–121 (2016). [https://doi.org/10.1016/0550-3213\(74\)90182-5](https://doi.org/10.1016/0550-3213(74)90182-5)
3. J.A. Wheeler, Molecular viewpoints in nuclear structure. *Phys. Rev.* **52**, 1083 (1937). <https://doi.org/10.1103/PhysRev.52.1083>
4. H. Margenau, Interaction of alpha-particles. *Phys. Rev.* **59**, 37–47 (1941). <https://doi.org/10.1103/PhysRev.59.37>
5. L.R. Hafstad, E. Teller, The alpha-particle model of the nucleus. *Phys. Rev.* **54**, 681 (1938). <https://doi.org/10.1103/PhysRev.54.681>
6. K. Ikeda, N. Takigawa, H. Horiuchi, The systematic structure-change into the molecule-like structures in the self-conjugate 4n nuclei. *Prog. Theor. Phys. Suppl.* **68**, 464 (1968). <https://doi.org/10.1143/PTPS.E68.464>
7. W. Oertzen, M. Freer, Y. Kanada-En'yo, Nuclear clusters and nuclear molecules. *Phys. Rep.* **432**, 43–113 (2006). <https://doi.org/10.1016/j.physrep.2006.07.001>
8. H. Horiuchi, K. Ikeda, K. Katō, Recent developments in nuclear cluster physics. *Prog. Theor. Phys. Suppl.* **192**, 1–238 (2012). <https://doi.org/10.1143/PTPS.192.1>
9. B. Zhou, Y. Funaki, H. Horiuchi et al., Nonlocalized clustering: a new concept in nuclear cluster structure physics. *Phys. Rev. Lett.* **110**, 262501 (2013). <https://doi.org/10.1103/PhysRevLett.110.262501>
10. S. Kubono, Dam N. Binh, S. Hayakawa et al., Nuclear clusters in astrophysics. *Nucl. Phys. A* **834**, 647c–650c (2010). <https://doi.org/10.1016/j.nuclphysa.2010.01.113>
11. F. Hoyle, On nuclear reactions occurring in very hot STARS. I. The synthesis of elements from carbon to nickel. *Astrophys. J. Suppl. Ser.* **1**, 121 (1954). <https://doi.org/10.1086/190005>
12. H. Horiuchi, K. Ikeda, A molecule-like structure in atomic nuclei of $^{16}\text{O}^*$ and ^{20}Ne . *Prog. Theo. Phys.* **40**, 277–287 (1968). <https://doi.org/10.1143/PTP.40.277>
13. M. Freer, The clustered nucleus-cluster structures in stable and unstable nuclei. *Rep. Prog. Phys.* **70**, 2149 (2007). <https://doi.org/10.1088/0034-4885/70/12/R03>
14. Y.L. Ye, L.H. Lyu, Z.X. Cao et al., Probing the halo and cluster structure of exotic nuclei. *Chin. Phys. C* **36**, 127–131 (2012). <https://doi.org/10.1088/1674-1137/36/2/004>
15. Y. Kanada-En'yo, M. Kimura, A. Ono, Antisymmetrized molecular dynamics and its applications to cluster phenomena. *Prog. Theor. Exp. Phys.* **2012**, 01A202 (2012). <https://doi.org/10.1093/ptep/pts001>
16. R.S. Mulliken, Electronic population analysis on LCAO-MO molecular wave functions. II. Overlap populations, bond orders, and covalent bond energies. *J. Chem. Phys.* **23**, 1841–1846 (1955). <https://doi.org/10.1063/1.1740589>
17. Y. Abe, J. Hiura, H. Tanaka, On the stability of α -cluster structures in ^8Be and ^{12}C nuclei. *Prog. Theor. Phys.* **46**, 352–354 (1971). <https://doi.org/10.1143/PTP.46.352>
18. Y. Kanada-En'yo, M. Kimura, F. Kobayashi et al., Cluster structures in stable and unstable nuclei. *Nucl. Sci. Tech.* **26**, S20501 (2015). <https://doi.org/10.13538/j.1001-8042/nst.26.S20501>
19. M. Aygun, Z. Aygun, A theoretical study on different cluster configurations of the ^9Be nucleus by using a simple cluster model. *Nucl. Sci. Tech.* **28**, 86 (2017). <https://doi.org/10.1007/s41365-017-0239-2>
20. M.J. Lyu, K. Yoshida, Y. Kanada-En'yo et al., Manifestation of α clustering in ^{10}Be via α -knockout reaction. *Phys. Rev. C* **97**, 044612 (2018). <https://doi.org/10.1103/PhysRevC.97.044612>
21. S. Okabe, Y. Abe, H. Tanaka, The structure of ^9Be nucleus by a molecular model. I. *Prog. Theor. Phys.* **57**, 866–881 (1977). <https://doi.org/10.1143/PTP.57.866>
22. W. Oertzen, Two-center molecular states in ^9B , ^9Be , ^{10}Be , and ^{11}Be . *Z. Phys. A* **354**, 37–43 (1996). <https://doi.org/10.1007/s002180050010>
23. N. Itagaki, S. Okabe, Molecular orbital structures in ^{10}Be . *Phys. Rev. C* **61**, 044306 (2000). <https://doi.org/10.1103/PhysRevC.61.044306>
24. M. Ito, N. Itagaki, H. Sakurai et al., Coexistence of covalent superdeformation and molecular resonances in an unbound region

- of ^{12}Be . Phys. Rev. Lett. **100**, 182502 (2008). <https://doi.org/10.1103/PhysRevLett.100.182502>
25. M. Ito, Formations of loose clusters in an unbound region of ^{12}Be . Phys. Rev. C **85**, 044308 (2012). <https://doi.org/10.1103/PhysRevC.85.044308>
 26. Z.H. Yang, Y.L. Ye, Z.H. Li et al., Observation of enhanced monopole strength and clustering in ^{12}Be . Phys. Rev. Lett. **112**, 162501 (2014). <https://doi.org/10.1103/PhysRevLett.112.162501>
 27. Z.H. Yang, Y.L. Ye, Z.H. Li et al., Helium–helium clustering states in ^{12}Be . Phys. Rev. C **91**, 024304 (2015). <https://doi.org/10.1103/PhysRevC.91.024304>
 28. Z.H. Yang, Y.L. Ye, Z.H. Li et al., Determination of the cluster spectroscopic factor of the 10.3 MeV state in ^{12}Be . Sci. Chin. Phys. **57**, 1613–1617 (2014). <https://doi.org/10.1007/s11433-014-5555-5>
 29. W. Jiang, Y.L. Ye, Z.H. Li et al., High-lying excited states in ^{10}Be from the $^9\text{Be}(^9\text{Be}, ^{10}\text{Be})^8\text{Be}$ reaction. Sci. Chin. Phys. **60**, 062011 (2017). <https://doi.org/10.1007/s11433-017-9023-x>
 30. M. Freer, J.C. Angélique, L. Axelsson et al., Exotic molecular states in ^{12}Be . Phys. Rev. Lett. **82**, 1383–1386 (1999). <https://doi.org/10.1103/PhysRevLett.82.1383>
 31. M. Freer, J.C. Angélique, L. Axelsson et al., Helium breakup states in ^{10}Be and ^{12}Be . Phys. Rev. C **63**, 034301 (2001). <https://doi.org/10.1103/PhysRevC.63.034301>
 32. J.A. Liendo, N. Curtis, D.D. Caussyn et al., Near threshold three-body final states in $^7\text{Li}+^7\text{Li}$ reactions at $E_{\text{lab}} = 34\text{MeV}$. Phys. Rev. C **65**, 034317 (2002). <https://doi.org/10.1103/PhysRevC.65.034317>
 33. W. Oertzen, Dimers based on the $\alpha + \alpha$ potential and chain states of carbon isotopes. Z. Phys. A **357**, 355–365 (1997). <https://doi.org/10.1007/s002180050255>
 34. Y. Kanada-En'yo, The structure of ground and excited states of ^{12}C . Prog. Theor. Phys. **117**, 655–680 (2007). <https://doi.org/10.1143/PTP.117.655>
 35. N. Itagaki, S. Okabe, K. Ikeda et al., Molecular-orbital structure in neutron-rich C isotopes. Phys. Rev. C **64**, 014301 (2001). <https://doi.org/10.1103/PhysRevC.64.014301>
 36. M. Freer, J.D. Malcolm, N.L. Achouri et al., Resonances in ^{14}C observed in the $^4\text{He}(^{10}\text{Be}, \alpha)^{10}\text{Be}$ reaction. Phys. Rev. C **90**, 054324 (2014). <https://doi.org/10.1103/PhysRevC.90.054324>
 37. Z.Y. Tian, Y.L. Ye, Z.H. Li et al., Cluster decay of the high-lying excited states in ^{14}C . Chin. Phys. C **40**, 111001 (2016). <https://doi.org/10.1088/1674-1137/40/11/111001>
 38. J. Li, Y.L. Ye, Z.H. Li et al., Selective decay from a candidate of the σ -bond linear-chain state in ^{14}C . Phys. Rev. C **95**, 021303 (2017). <https://doi.org/10.1103/PhysRevC.95.021303>
 39. H.L. Zang, Y.L. Ye, Z.H. Li et al., Investigation of the near-threshold cluster resonance in ^{14}C . Chin. Phys. C **42**, 074003 (2018). <https://doi.org/10.1088/1674-1137/42/7/074003>
 40. J. Feng, Y.L. Ye, B. Yang et al., Enhanced monopole transition strength from the cluster decay of ^{13}C . Sci. Chin. Phys. **62**, 12011 (2018). <https://doi.org/10.1007/s11433-018-9258-7>
 41. T. Baba, M. Kimura, Structure and decay pattern of the linear-chain state in ^{14}C . Phys. Rev. C **94**, 044303 (2016). <https://doi.org/10.1103/PhysRevC.94.044303>
 42. T. Baba, M. Kimura, Characteristic α and ^6He decays of linear-chain structures in ^{16}C . Phys. Rev. C **97**, 054315 (2018). <https://doi.org/10.1103/PhysRevC.97.054315>
 43. D. Dell'Aquila, I. Lombardo, L. Acosta et al., New experimental investigation of the structure of ^{10}Be and ^{16}C by means of intermediate-energy sequential breakup. Phys. Rev. C **93**, 024611 (2016). <https://doi.org/10.1103/PhysRevC.93.024611>
 44. D.R. Thompson, M. Lemere, Y.C. Tang, Systematic investigation of scattering problems with the resonating-group method. Nucl. Phys. A **286**, 53–66 (1977). [https://doi.org/10.1016/0375-9474\(77\)90007-0](https://doi.org/10.1016/0375-9474(77)90007-0)
 45. S. Saito, I.I. Chapter, Theory of resonating group method and generator coordinate method, and orthogonality condition model. Prog. Theor. Phys. Suppl. **62**, 11–89 (1977). <https://doi.org/10.1143/PTPS.62.11>
 46. Y. Funaki, H. Horiuchi, A. Tohsaki, Cluster models from RGM to alpha condensation and beyond. Prog. Part. Nucl. Phys. **82**, 78–132 (2015). <https://doi.org/10.1016/j.pnpnp.2015.01.001>
 47. K. Wildermuth, E.J. Kanellopoulos, Clustering aspects in nuclei and their microscopic description. Rep. Prog. Phys. **42**, 1719 (1979). <https://doi.org/10.1088/0034-4885/42/10/003>
 48. Y.C. Tang, M. LeMere, D.R. Thompson, Resonating-group method for nuclear many-body problems. Phys. Rep. **47**, 167–223 (1978). [https://doi.org/10.1016/0370-1573\(78\)90175-8](https://doi.org/10.1016/0370-1573(78)90175-8)
 49. W.E. Hunt, M.K. Mehta, R.H. Davis, Scattering of alpha particles by oxygen. I. Bombarding energy range 5.8 to 10.0 MeV. Phys. Rev. **160**, 782 (1967). <https://doi.org/10.1103/PhysRev.160.782>
 50. D.L. Hill, J.A. Wheeler, Nuclear constitution and the interpretation of fission phenomena. Phys. Rev. **89**, 1102–1145 (1953). <https://doi.org/10.1103/PhysRev.89.1102>
 51. H.A. Bethe, Kinetic energy of nuclei in the Hartree model. Phys. Rev. **51**, 283 (1937). <https://doi.org/10.1103/PhysRev.51.283>
 52. P. Descouvemont, D. Baye, The ^{20}F and ^{20}N nuclei and the $^{19}\text{Ne}(p, \gamma)^{20}\text{Na}$ reaction in a microscopic three-cluster model. Nucl. Phys. A **517**, 143–158 (1990). [https://doi.org/10.1016/0375-9474\(90\)90265-N](https://doi.org/10.1016/0375-9474(90)90265-N)
 53. P. Descouvemont, Microscopic study of α clustering in the $^{9,10,11}\text{Be}$ isotopes. Nucl. Phys. A **699**, 463–478 (2002). [https://doi.org/10.1016/S0375-9474\(01\)01286-6](https://doi.org/10.1016/S0375-9474(01)01286-6)
 54. P. Descouvemont, D. Baye, ^{12}Be molecular states in a microscopic cluster model. Phys. Lett. B **505**, 71–74 (2001). [https://doi.org/10.1016/S0370-2693\(01\)00349-5](https://doi.org/10.1016/S0370-2693(01)00349-5)
 55. S. Saito, Interaction between clusters and Pauli principle. Prog. Theor. Phys. **41**, 705–722 (1969). <https://doi.org/10.1143/PTP.41.705>
 56. T. Matsuse, M. Kamimura, A study of α -widths of ^{20}Ne based on ^{16}O and α -cluster model. Prog. Theor. Phys. **49**, 1765–1767 (1973). <https://doi.org/10.1143/PTP.49.1765>
 57. H. Horiuchi, Many-cluster problem by the orthogonality condition model: general discussion and ^{12}C problem. Prog. Theor. Phys. **53**, 447–460 (1975). <https://doi.org/10.1143/PTP.53.447>
 58. H. Horiuchi, Generator coordinate theory of allowed states of many-cluster systems. Prog. Theor. Phys. **55**, 1448–1461 (1976). <https://doi.org/10.1143/PTP.55.1448>
 59. T. Yamada, Y. Funaki, α -cluster structures and monopole excitations in ^{13}C . Phys. Rev. C **92**, 034326 (2015). <https://doi.org/10.1103/PhysRevC.92.034326>
 60. T. Yamada, Y. Funaki, H. Horiuchi et al., Monopole excitation to cluster states. Prog. Theor. Phys. **120**, 1139 (2008). <https://doi.org/10.1143/PTP.120.1139>
 61. S. Okabe, Y. Abe, The structure of ^9Be nucleus by a molecular model. II. Prog. Theor. Phys. **61**, 1049–1064 (1979). <https://doi.org/10.1143/PTP.61.1049>
 62. M. Ito, K. Kato, K. Ikeda, Application of the generalized two-center cluster model to ^{10}Be . Phys. Lett. B **588**, 43–48 (2004). <https://doi.org/10.1016/j.physletb.2004.01.090>
 63. M. Ito, N. Itagaki, Covalent isomeric state in ^{12}Be induced by two-neutron transfers. Phys. Rev. C **78**, 011602 (2008). <https://doi.org/10.1103/PhysRevC.78.011602>
 64. M. Freer, N.I. Ashwood, N.L. Achouri et al., Elastic scattering of $^8\text{He} + ^4\text{He}$ and two-neutron transfer and the influence of resonances in ^{12}Be . Phys. Lett. B **775**, 58 (2017). <https://doi.org/10.1016/j.physletb.2017.10.063>

65. Y. Kanada-En'yo, H. Horiuchi, A. Ono, Structure of Li and Be isotopes studied with antisymmetrized molecular dynamics. *Phys. Rev. C* **52**, 628 (1995). <https://doi.org/10.1103/PhysRevC.52.628>
66. Y. Kanada-En'yo, Variation after angular momentum projection for the study of excited states based on antisymmetrized molecular dynamics. *Phys. Rev. Lett.* **81**, 5291–5293 (1998). <https://doi.org/10.1103/PhysRevLett.81.5291>
67. Y. Kanada-En'yo, H. Horiuchi, Structure of light unstable nuclei studied with antisymmetrized molecular dynamics. *Prog. Theor. Phys. Suppl.* **142**, 205 (2001). <https://doi.org/10.1143/PTPS.142.205>
68. Y. Kanada-En'yo, H. Horiuchi, A. Doté, Structure of excited states of ^{10}Be studied with antisymmetrized molecular dynamics. *Phys. Rev. C* **60**, 064304 (1999). <https://doi.org/10.1103/PhysRevC.60.064304>
69. Y. Kanada-En'yo, H. Horiuchi, Cluster structures of the ground and excited states of ^{12}Be studied with antisymmetrized molecular dynamics. *Phys. Rev. C* **68**, 014319 (2003). <https://doi.org/10.1103/PhysRevC.68.014319>
70. Y. Kanada-En'yo, M. Kimura, H. Horiuchi, Antisymmetrized molecular dynamics: a new insight into the structure of nuclei. *C. R. Phys.* **4**, 497–520 (2003). [https://doi.org/10.1016/S1631-0705\(03\)00062-8](https://doi.org/10.1016/S1631-0705(03)00062-8)
71. A. Doté, H. Horiuchi, Y. Kanada-En'yo, Antisymmetrized molecular dynamics plus Hartree–Fock model and its application to Be isotopes. *Phys. Rev. C* **56**, 1844–1854 (1997). <https://doi.org/10.1103/PhysRevC.56.1844>
72. T. Baba, Y. Chiba, M. Kimura, 3α clustering in excited states of ^{16}C . *Phys. Rev. C* **90**, 064319 (2014). <https://doi.org/10.1103/PhysRevC.90.064319>
73. T. Baba, M. Kimura, Three-body decay of linear-chain states in ^{14}C . *Phys. Rev. C* **95**, 064318 (2017). <https://doi.org/10.1103/PhysRevC.95.064318>
74. A. Fritsch, S. Beceiro-Novo, D. Suzuki et al., One-dimensionality in atomic nuclei: a candidate for linear-chain α clustering in ^{14}C . *Phys. Rev. C* **93**, 014321 (2016). <https://doi.org/10.1103/PhysRevC.93.014321>
75. P. Arumugam, B.K. Sharma, S.K. Patra et al., Relativistic mean field study of clustering in light nuclei. *Phys. Rev. C* **71**, 064308 (2005). <https://doi.org/10.1103/PhysRevC.71.064308>
76. L. Morelli, M. D'Agostino, M. Bruno et al., Clustering effects in fusion evaporation reactions with light even–even $N = Z$ nuclei. *J. Phys. Conf. Ser.* **863**, 012022 (2017). <https://doi.org/10.1088/1742-6596/863/1/012022>
77. D.L. Price, M. Freer, N.I. Ashwood et al., α decay of excited states in ^{14}C . *Phys. Rev. C* **75**, 014305 (2007). <https://doi.org/10.1103/PhysRevC.75.014305>
78. W. Oertzen, H.G. Bohlen et al., Search for cluster structure of excited states in ^{14}C . *Eur. Phys. J. A* **21**, 193–215 (2004). <https://doi.org/10.1140/epja/i2003-10188-9>
79. H. Takemoto, H. Horiuchi, A. Ono, Incident-energy dependence of the fragmentation mechanism reflecting the cluster structure of the ^{19}B nucleus. *Phys. Rev. C* **63**, 034615 (2001). <https://doi.org/10.1103/PhysRevC.63.034615>
80. R. Qiao, Y.L. Ye, J. Wang et al., A new uniform calibration method for double-sided silicon strip detectors. *IEEE Trans. Nucl. Sci.* **61**, 596–601 (2014). <https://doi.org/10.1109/TNS.2013.2295519>
81. R.J. Charity, S.A. Komarov, L.G. Sobotka et al., Particle decay of ^{12}Be excited states. *Phys. Rev. C* **76**, 064313 (2007). <https://doi.org/10.1103/PhysRevC.76.064313>
82. Z.X. Cao, Y.L. Ye, J. Xiao et al., Recoil proton tagged knockout reaction for ^8He . *Phys. Lett. B* **707**, 46–51 (2012). <https://doi.org/10.1016/j.physletb.2011.12.009>
83. A.A. Korshennikov, E.Y. Nikolskii, T. Kobayashi et al., Spectroscopy of ^{12}Be and ^{13}Be using a ^{12}Be radioactive beam. *Phys. Lett. B* **343**, 53–58 (1995). [https://doi.org/10.1016/0370-2693\(94\)01435-F](https://doi.org/10.1016/0370-2693(94)01435-F)
84. A.M. Lane, R.G. Thomas, R-matrix theory of nuclear reactions. *Rev. Mod. Phys.* **30**, 257 (1958). <https://doi.org/10.1103/RevModPhys.30.257>
85. M. Freer, E. Casarejos, L. Achouri et al., $\alpha : 2n : \alpha$ Molecular band in ^{10}Be . *Phys. Rev. Lett.* **96**, 042501 (2006). <https://doi.org/10.1103/PhysRevLett.96.042501>
86. M. Itoh, H. Sakaguchi, M. Uchida et al., Compressional-mode giant resonances in deformed nuclei. *Phys. Lett. B* **549**, 58–63 (2002). [https://doi.org/10.1016/S0370-2693\(02\)02892-7](https://doi.org/10.1016/S0370-2693(02)02892-7)
87. D.J. Horen, J.R. Beene, G.R. Satchler, Folded potential analysis of the excitation of giant resonances by heavy ions. *Phys. Rev. C* **52**, 1554–1564 (1995). <https://doi.org/10.1103/PhysRevC.52.1554>
88. I.J. Thompson, Coupled reaction channels calculations in nuclear physics. *Comput. Phys. Rep.* **7**, 167–212 (1988). [https://doi.org/10.1016/0167-7977\(88\)90005-6](https://doi.org/10.1016/0167-7977(88)90005-6)
89. N.I. Ashwood, N.M. Clarke, M. Freer, ^{10}Be excited states populated in the $^9\text{Be}(^9\text{Be}, ^8\text{Be})^{10}\text{Be}$ reaction. *Phys. Rev. C* **68**, 017603 (2003). <https://doi.org/10.1103/PhysRevC.68.017603>
90. H.G. Bohlen, W. von Oertzen, R. Kalpakchieva et al., Structure of neutron-rich Be and C isotopes. *Phys. Atom. Nucl.* **66**, 1494–1500 (2003). <https://doi.org/10.1134/1.1601755>
91. N. Soić, M. Freer, L. Donadille et al., ^4He decay of excited states in ^{14}C . *Phys. Rev. C* **68**, 014321 (2003). <https://doi.org/10.1103/PhysRevC.68.014321>
92. J. Walshe, M. Freer, C. Wheldon et al., The thick target inverse kinematics technique with a large acceptance silicon detector array. *J. Phys. Conf. Ser.* **569**, 012052 (2014). <https://doi.org/10.1088/1742-6596/569/1/012052>
93. D. Suzuki, M. Ford, D. Bazin et al., Prototype AT-TPC: toward a new generation active target time projection chamber for radioactive beam experiments. *Nucl. Inst. Methods A* **691**, 39–54 (2012). <https://doi.org/10.1016/j.nima.2012.06.050>
94. H. Yamaguchi, D. Kahl, S. Hayakawa et al., Experimental investigation of a linear-chain structure in the nucleus ^{14}C . *Phys. Lett. B* **766**, 11–16 (2017). <https://doi.org/10.1016/j.physletb.2016.12.050>
95. T. Suhara, Y. Kanada-En'yo, Cluster structures of excited states in ^{14}C . *Phys. Rev. C* **82**, 044301 (2010). <https://doi.org/10.1103/PhysRevC.82.044301>
96. Q. Liu, Y.L. Ye, Z.H. Li et al., Investigation of the thickness non-uniformity of the very thin silicon-strip detectors. *Nucl. Inst. Methods A* **897**, 100–105 (2018). <https://doi.org/10.1016/j.nima.2018.04.041>